

TNI	Kozmická technika Príručka pre tepelnotechnický návrh Časť 14: Kryogénne chladenie	TNI CEN/CLC/TR 17603-31-14 31 0540
------------	---	--

Space Engineering - Thermal design handbook - Part 14: Cryogenic Cooling

Táto technická normalizačná informácia obsahuje anglickú verziu CEN/CLC/TR 17603-31-14:2021.
This Technical standard information includes the English version of CEN/CLC/TR 17603-31-14:2021.

Táto technická normalizačná informácia bola oznámená vo Vestníku ÚNMS SR č. 12/21

134178

TECHNICAL REPORT
RAPPORT TECHNIQUE
TECHNISCHER BERICHT

**CEN/CLC/TR 17603-31-
14**

August 2021

ICS 49.140

English version

**Space Engineering - Thermal design handbook - Part 14:
Cryogenic Cooling**

Ingénierie spatiale - Manuel de conception thermique -
Partie 14 : Refroidissement cryogénique

Raumfahrttechnik - Handbuch für thermisches Design -
Teil 14: Kryogene

This Technical Report was approved by CEN on 28 June 2021. It has been drawn up by the Technical Committee CEN/CLC/JTC 5.

CEN and CENELEC members are the national standards bodies and national electrotechnical committees of Austria, Belgium, Bulgaria, Croatia, Cyprus, Czech Republic, Denmark, Estonia, Finland, France, Germany, Greece, Hungary, Iceland, Ireland, Italy, Latvia, Lithuania, Luxembourg, Malta, Netherlands, Norway, Poland, Portugal, Republic of North Macedonia, Romania, Serbia, Slovakia, Slovenia, Spain, Sweden, Switzerland, Turkey and United Kingdom.



**CEN-CENELEC Management Centre:
Rue de la Science 23, B-1040 Brussels**

Table of contents

European Foreword	25
1 Scope	26
2 References	27
3 Terms, definitions and symbols	28
3.1 Terms and definitions	28
3.2 Abbreviated terms.....	28
3.3 Symbols.....	30
4 General introduction	42
4.1 Radiant coolers.....	43
4.2 Stored solid-cryogen coolers	44
4.3 Stored liquid Helium (He4) coolers	44
4.4 Trends toward lower temperatures	45
4.5 Mechanical refrigerators	46
4.6 Low temperature requirements to IR sensors	47
4.6.2 Radiation from the optical system	48
4.6.3 Noise from the detector	49
5 Refrigerating systems	51
5.1 General.....	51
5.2 Closed cycle	51
5.2.1 Reverse-Brayton cycle	52
5.2.2 Reverse-Brayton and Claude cycle refrigerators	54
5.2.3 Gifford-McMahon/Solvay cycle refrigerators.....	55
5.2.4 Joule-Thomson Closed Cycle Refrigerator	57
5.2.5 Stirling cycle refrigerators.....	58
5.2.6 Vuilleumier cycle refrigerator	66
5.2.7 Existing systems	69
5.3 Open cycle	105
5.3.1 Joule-Thomson open cycle refrigerators	105
5.3.2 Existing systems	108

CEN/CLC/TR 17603-31-14:2021 (E)

5.3.3	Stored liquid or solid cryogen open refrigerators	114
6	VCS Dewars	115
6.1	General.....	115
6.2	Theoretical analysis	117
6.2.1	Introduction	117
6.2.2	The idealized model	118
6.2.3	Evaluation of the restrictions involved in the idealized model	123
6.3	Supports	162
6.3.1	Introduction	162
6.3.2	Support materials	163
6.3.3	Low thermal conductance tubing	165
6.3.4	Tensile and flexural supports	170
6.3.5	Compressive supports	175
6.4	Phase separators	176
6.4.1	Introduction	176
6.4.2	Thermodynamic vent system	182
6.4.3	Capillary barriers	183
6.4.4	Porous media	190
6.4.5	Baffled tanks	193
6.4.6	Empirical data for design.....	205
6.4.7	Testing	216
6.5	Existing systems	218
6.5.1	Introduction	218
6.5.2	Data on existing systems	220
7	Superfluid Helium	234
7.1	Dynamics of superfluids.....	234
7.1.1	Relevant equations of superfluid dynamics	235
7.1.2	Frictional effects	240
7.1.3	Counterflow heat transfer	246
7.1.4	Heat transfer at arbitrary combinations of v_n and v_s	257
7.1.5	Vapor formation	258
7.1.6	Superfluid Helium film	259
7.2	Kapitza conductance	267
7.2.1	Measuring methods.....	269
7.2.2	Experimental data	272
7.3	Thermo-acoustic oscillations.....	303
7.4	The superfluid plug	305

CEN/CLC/TR 17603-31-14:2021 (E)

7.4.1	Phase separation in superfluid helium.....	305
7.4.2	Simplified theory of the superfluid plug.....	306
7.4.3	Characteristics of porous media	330
7.5	Filling a superfluid helium container.....	338
7.5.1	Liquid loss because of pump down	338
7.5.2	Pumping down requirements.....	340
7.5.3	A typical filling sequence	340
8	Materials at cryogenic temperatures	343
8.1	Normal cryogenics	343
8.1.1	General properties	343
8.1.2	Entropy diagrams	391
8.2	Superfluid Helium-4	443
8.3	Normal Helium-3.....	449
8.4	Metallic materials.....	452
8.5	Composite materials.....	466
8.5.1	Structural tubes.....	493
8.6	Miscellaneous materials.....	495
9	Safety with cryogenic systems	496
9.1	General.....	496
9.1.1	Physiological hazards	496
9.1.2	Fire and explosion hazards	496
9.1.3	Pressure hazards.....	497
9.1.4	Materials hazards.....	497
9.1.5	Safety provisions.....	498
9.2	Hazards related to properties of cryogenics	499
9.2.1	Combustion in an oxygen environment	501
9.2.2	Combustible cryogenics.....	502
9.2.3	Fluorine.....	510
9.2.4	O ₂ deficiency.....	511
9.3	Change of properties of structural materials.....	511
9.3.1	Temperature embrittlement	511
9.3.2	Hydrogen embrittlement.....	521
9.3.3	Design codes and acceptance tests	528
	Bibliography.....	529

Figures

CEN/CLC/TR 17603-31-14:2021 (E)

Figure 4-1: He ³ cooler being developed by NASA. From Sherman (1978) [216].	46
Figure 4-2: Procedure to reduce the background flux from the optics. From Caren & Sklensky (1970) [37].	48
Figure 4-3: Detectivity, D^* , of a photon noise-limited detector as a function of cutoff wavelength, λ_c , for several values of the optics temperature, T . From Caren & Sklensky (1970) [37].	49
Figure 4-4: Typical detector operating temperature, T , vs. detectivity, D^* . The detector is germanium doped either with mercury, with cadmium or with copper. From Caren & Sklensky (1970) [37].	50
Figure 5-1: Reverse-Brayton Cycle Refrigerator. From Sherman (1978) [216].	52
Figure 5-2: Compressor cross section of ADL rotary-reciprocating refrigerator. From Donabedian (1972) [59].	53
Figure 5-3: Claude Cycle Refrigerator. From Donabedian (1972) [59].	54
Figure 5-4: Solvay Cycle Refrigerator. From Donabedian (1972) [59].	56
Figure 5-5: Joule-Thomson Closed Cycle Refrigerator. From Donabedian (1972) [59].	57
Figure 5-6: Stirling Cycle Refrigerator Operation. From Sherman (1978) [216].	58
Figure 5-7: Stirling Cycle Refrigerator Ideal Pressure-Volume and Temperature-Entropy Diagrams. From Sherman (1978) [216].	59
Figure 5-8: Schematic representation of North American Philips refrigerator, showing rhombic drive mechanism. The drive has two counter-rotating crankshafts, each powered by a drive motor. By adjusting the mass of the reciprocating members of the drive and by adding appropriate counterweights to the crankshafts, the center of the gravity of all the moving parts can be kept stationary. From Balas, Leffel & Wingate (1978) [16].	60
Figure 5-9: Schematic representation of North American Philips Magnetic Bearing refrigerator, showing the linear motors for piston and displacer and the magnetic bearing. The displacer rod passes through the piston. From Sherman, Gasser, Benson & McCormick (1980) [221].	61
Figure 5-10: Coupling of two refrigerator units to provide cooling of a single detector. The complete refrigerator can be seen in Figure 5-8. Here, on the contrary, only the first and second stages of both refrigerators are shown. From Naes & Nast (1980) [160].	62
Figure 5-11: Ground Test temperatures, of the first and second stage vs. Second stage heat transfer rate, Q_2 , for different values of the first stage heat transfer rate, Q_1 , and motor rpm. The data correspond to refrigerator 2 but are typical of the four units. From Naes & Nast (1980) [160]. ○ first stage, $Q_1 = 1,5$ W, 1000 rpm; □ first stage, $Q_1 = 1,5$ W, 1150 rpm; △ second stage $Q_1 = 1,5$ W, 1000 rpm; ▽ second stage $Q_1 = 1,5$ W, 1150 rpm; ▷ first stage, $Q_1 = 2$ W, 1000 rpm; ◁ $Q_1 = 2$ W, 1000 rpm.	63
Figure 5-12: In orbit temperature, T , of several components of Gamma 004 systems vs. Orbital time, t . From Naes & Nast (1980) [160]. ○ cold tip of refrigerator 3; □ cold tip of refrigerator 4; △ shroud; ● ground test value of cold tip of refrigerator 3; ▲ ground test value of shroud.	63
Figure 5-13: In orbit temperature, T , of several components of Gamma 003 systems vs. Orbital time, t . From Naes & Nast (1980) [160]. ○ cold tip of refrigerator 2; □ cold tip of refrigerator 1; △ shroud; ● ground test value of cold tip of refrigerator 2; ▲ ground test value of shroud.	64

CEN/CLC/TR 17603-31-14:2021 (E)

Figure 5-14: In orbit heat transfer rates, Q , from Gamma 003 detector to refrigerators 1 and 2, vs. orbital time, t . From Naes & Nast (1980) [160]. ○ detector heat load. Refrigerator 2 on; □ heat load through meter 1, Q_1 . Refrigerator 1 off; △ heat load through meter 2, Q_2 . Refrigerator 2 on; ● refrigerators 1 and 2 on; ■ refrigerators 1 and 2 on; ▲ refrigerators 1 and 2 on.	64
Figure 5-15: Schematic of the Vuilleumier-Cycle Refrigerator. From Sherman (1978) [216].	67
Figure 5-16: Vuilleumier-Cycle Refrigerator. From Sherman (1971) [218].	67
Figure 5-17: Pressure-Volume Diagrams, for the Cold Cylinder, Hot Cylinder and Total Gas, of the Vuilleumier-Cycle Refrigerator. From Sherman (1971) [218].	67
Figure 5-18: Inverse efficiency (required power per unit of refrigeration power) η^{-1} , vs. operating temperature, T , for several closed cycle refrigerators. a - Brayton refrigerators (Turbo machinery Systems). b - Stirling refrigerators. c - Vuilleumier refrigerators. d - Gifford-McMahon/Solvay refrigerators. From Donabedian (1972) [59]. Also shown are curves for closed cycle refrigerators operating with the quoted efficiencies (in percentages of Carnot) through the whole temperature range. From Haskin & Dexter (1979) [83]. The Carnot efficiency for a machine working between T_C and T_H temperatures is given by $\eta_c = 1 - T_C/T_H$. Very low operating temperatures result in a reduced efficiency for a given cooling load and a given cycle.	70
Figure 5-19: System mass per unit of refrigeration power, M_p , vs. operating temperature, T for several closed cycle refrigerators. a - Gifford-McMahon/Solvay refrigerators. b - Stirling refrigerators. From Donabedian (1972) [59].	71
Figure 5-20: System mass per unit of refrigeration power (or cooling load), M_p , for representative closed cycle refrigerating systems and for passive radiant coolers. ○ Closed cycle refrigerators, $Q = 0,1$ W. ● Closed cycle refrigerators, $Q = 1$ W. ● Closed cycle refrigerators, $Q = 10$ W. □ Passive radiant coolers; $Q = 0,1$ W. ■ Passive radiant coolers; $Q = 1$ W. ■ Passive radiant coolers; $Q = 10$ W. From Haskin & Dexter (1979) [83]. ▨ Smallest temperature attained by closed cycle refrigerators in orbit. ▩ Smallest temperature attained by passive radiant coolers in orbit. From Sherman (1982) [217].	72
Figure 5-21: System area per unit of refrigeration power (or cooling load), A_p/M_p , for closed cycle refrigerating systems and for passive radiant coolers. ○ Closed cycle refrigerators, $Q = 1$ W. □ Passive radiant coolers; $Q = 1$ W. From Haskin & Dexter (1979) [83]. Although the areas, A_p , have been calculated for 1 W cooling, they could be scaled in approximately direct proportion to the cooling load. $A_p/Q = 7,13 \times 10^7 T^{-4}$ is the best fitting, by the least squares method, to the data for passive radiant coolers. ▨ Smallest temperature attained by closed cycle refrigerators in orbit. ▩ Smallest temperature attained by passive radiant coolers in orbit. From Sherman (1982) [217].	75
Figure 5-22: 80 K cooler schematic. From Jewell (1991) [103].	101
Figure 5-23: Cooler heat lift performance vs. gross compressor input power. From Scull & Jewell (1991) [211].	102
Figure 5-24: 20 K cooler schematic. From Jones et al. (1991) [110].	103

CEN/CLC/TR 17603-31-14:2021 (E)

Figure 5-25: Heat lift performance of: a) development model; b) engineering model. From Jones et al. (1991) [110].	104
Figure 5-26: 4 K cooler layout. From Bradshaw & Orłowska (1988) [27].	104
Figure 5-27: Cooling power/mass flow vs. precooler temperature. From Bradshaw & Orłowska (1991) [28].	105
Figure 5-28: Isenthalps and inversion curve for different gasses. a Hydrogen. b Helium. c Nitrogen. From Zemansky (1968) [272]. Data in b, after Hill & Loumasmaa (1960) [89], are no longer valid for above 20 K. Upper isenthalps are instead from Angus & de Reuck (1977) [6], pp. 64-127. The locus of the maxima has been drawn by the compiler as a dotted line.	106
Figure 5-29: Schematic of a typical JT cryostat-dewar system. From Hellwig (1980) [86].	107
Figure 5-30: Schematic of a self-demand flow JT cryostat-dewar system. From Oren & Gutfinger (1979) [175]. The sketch of the variable-orifice controlling device is from Buller (1970) [35].	108
Figure 6-1: Schematic representation of a solid groygen cooler. From Breckenridge (1972) [29].	116
Figure 6-2: Sketch of a typical VCS Dewar. From Niendorf & Choksi (1967) [169].	117
Figure 6-3: Heat transfer mechanism through a normal attachment VCS Dewar. From Niendorf & Choksi (1967) [169].	117
Figure 6-4: Insulation model geometry.	119
Figure 6-5: Ratio m/m_0 against the cryogen sensibility, S , for different values of the heat additions to the cryogen other than those across the insulation. No cooled supports ($m_{sj} = 0$). Calculated by the compiler.	121
Figure 6-6: Corrective factor, ω_k , for the dependence of insulation thermal conductivity, k , on temperature, T , against the sensibility, S , of the cryogen, for several values of the temperature ratio, T_C/T_H . A linear thermal conductivity vs. temperature dependence has been assumed. Calculated by the compiler.	128
Figure 6-7: Insulation model with finite number of shields.	129
Figure 6-8: Corrective factor, ω_n , accounting for the influence of the finite number, n , of shields, vs. the sensibility S of the cryogen, for several values of n . Calculated by the compiler.	134
Figure 6-9: Contours of constant values of the ratio of the heat flux through the VCS system to the uncooled shield heat flux, mapped as functions of the dimensionless distances, ξ_1 and ξ_2 , of the two vapor cooled shields to the cold face of the insulation, for several values of the sensibility, S , of the cryogen. Uniform insulation thermal conductivity. The numerical values labelling the contours corresponds to $\omega_n/\omega_{nopt} - 1$. Calculated by the compiler.	140
Figure 6-10: Contours of dimensionless displacements of a single shield from its optimum position ($\xi_1 = 0,25$) which produce a 10% increase in the heat flux through a three shield system. The contours are mapped as functions of the remaining two shields dimensionless positions. Numerical values are for helium between 4 K and 300 K. From Atherton & Prentiss (1973) [12].	141
Figure 6-11: Contours of constant values of the ratio of the heat flux through the VCS system to the uncooled shield heat flux, mapped as functions of the dimensionless distances, ξ_1 and ξ_2 , of the two vapor cooled shields to the	

CEN/CLC/TR 17603-31-14:2021 (E)

<p>cold face of the insulation, for several cryogenes in typical cases. Temperature dependent insulation thermal conductivity ($k = k_1 T$). The numerical values labelling the contours corresponds to $\omega_H/\omega_{nopt} - 1$. Calculated by the compiler.</p>	142
Figure 6-12: Factor ω_{Nu} , accounting for finite convective heat transfer in the venting duct, vs. coefficient r , for several cryogenes. $T_H = 300$ K. Calculated by the compiler.	145
Figure 6-13: Factor ω_{Nu} , accounting for finite convective heat transfer in the venting duct, vs. coefficient r , for several cryogenes. $T_H = 200$ K. Calculated by the compiler.	146
Figure 6-14: Factor ω_{Nu} , accounting for finite convective heat transfer in the venting duct, vs. coefficient r , for several cryogenes. $T_H = 150$ K. Calculated by the compiler.	147
Figure 6-15: Helium vapor bulk temperature, T_b , vs. insulation temperature, T , for different values of the dimensionless heat transfer coefficient, r . $T_H = 300$ K. Calculated by the compiler.	148
Figure 6-16: Temperature, T , across the insulation for different values of the dimensionless heat transfer coefficient r . Helium vapor cooling. $T_H = 300$ K. Calculated by the compiler.	149
Figure 6-17: Sketch of a VCS insulation in the nearness of the venting duct. Normal attachment. After Paivanas et al. (1965) [177].	149
Figure 6-18: Sketch of the insulation and of the simplified configurations used to analyze the influence of the finite thermal conductivity of the shields. (a) Insulation. (b) Simplified configuration in the physical coordinates x, y . (c) Simplified configuration in the stretched coordinates, ξ, η	151
Figure 6-19: Sketch of a typical spaceborne Dewar. All the dimensions are in mm.	152
Figure 6-20: Coefficient, $(\omega_y - 1)/\varepsilon$, of the first order correction accounting for the influence of the finite thermal conductivity of the VCSs on the cryogen boil-off rate, as a function of the cryogen sensibility, S , for two values of the dimensionless outer radius of the venting duct, α . The results have been obtained by means of a perturbation scheme in the small parameter, ε , which measured the ratio of normal to lateral heat flux, and are valid provided that terms of order $\varepsilon^{3/2}$ can be neglected. Calculated by the compiler.	160
Figure 6-21: Cryogenic supports tubes. a) Composite. b) All-metal. All dimensions are in mm. From Hall & Spond (1977) [81].	166
Figure 6-22: Heat transfer rate, Q_s , through fiber-glass overwrapped and through all-stainless-steel supports vs. support length, L , for several values of liner wall thickness, t_l , and overwrap thickness, t_o . (a) Inner diameter of the tube, $d = 12,7 \times 10^{-3}$ m. (b) $d = 50,8 \times 10^{-3}$ m. From Hall et al. (1971) [80].	167
Figure 6-23: Heat transfer rate, Q_s , through fiber-glass overwrapped supports vs. liner wall thickness, t_l , for several support lengths, L and overwrap thickness, $t_o = 0,762 \times 10^{-3}$ m. Hoop wrapping. (a) Inner diameter of the tube, $d = 12,7 \times 10^{-3}$ m. (b) $d = 50,8 \times 10^{-3}$ m. From Hall et al. (1971) [80].	168
Figure 6-24: Heat transfer rate, Q_s , through fiber-glass overwrapped stainless-steel supports vs. overwrap thickness, t_o , for several supports lengths, L , and liner wall thickness $t_l = 0,51 \times 10^{-3}$ m. Hoop wrapping. (a) Inner diameter of the tube, $d = 12,7 \times 10^{-3}$ m. (b) $d = 50,8 \times 10^{-3}$ m. From Hall et al. (1971) [80].	169

CEN/CLC/TR 17603-31-14:2021 (E)

Figure 6-25: Heat transfer rate, Q_s , through fiber-glass overwrapped stainless-steel supports vs. warm boundary temperature, T_H , for several values of the cold boundary temperature, T_C . Tube length, L , liner wall thickness, t_l , and overwrap thickness, t_o , as indicated in the insert. Hoop wrapping. (a) Inner diameter of the tube, $d = 12,7 \times 10^{-3}$ m. (b) $d = 50,8 \times 10^{-3}$ m. From Hall et al. (1971) [80].	170
Figure 6-26: Typical supporting methods. Notice how the rods shown in (a) are crossed to minimize the effect of thermal contraction and to increase the length of the heat flow path. In (b), long suspension rods are accommodated in standoffs. From Barron (1966) [18].	171
Figure 6-27: Tensile support of a liquid helium tank. From Lemke, Klipping & Römisch (1978) [131].	171
Figure 6-28: Spacing discs. From Bennett et al. (1974) [23].	172
Figure 6-29: Support tube for a liquid helium Dewar. From Bennett et al. (1974) [23].	173
Figure 6-30: Two ways of supporting cryogenic containers by means of tensile ties. After Glaser et al. (1967) [75].	174
Figure 6-31: Sketch of the Superfluid Helium Cryostat for Space Use (CRHESUS) showing the tensile ties used for supporting the helium tank. From Lizon-Tati & Girard (1978) [134].	174
Figure 6-32: CRHESUS heat flow diagram. From Lizon-Tati & Girard (1978) [134].	175
Figure 6-33: Composite column compressive support. From Heim & Fast (1973) [85].	176
Figure 6-34: Schematic of thermodynamic vent system. a) Forced convection. From Mitchell et al. (1967). b) Pulsed constant pressure. From Müller et al. (1983) [157].	182
Figure 6-35: Thermodynamic phase separator. From Fradkov & Troitskii (1975) [71].	183
Figure 6-36: A capillary barrier in static equilibrium. From McCarthy (1968) [144].	184
Figure 6-37: Container with a capillary-barrier partition. From McCarthy (1968) [144]. (a) An angular acceleration appears when the interface is formed at the barrier. (b) The configuration reaches a steady angular velocity before interaction of the interface with the barrier. See Table 6-12 for the definition of the experimental conditions.	185
Figure 6-38: Results of barrier dynamic stability tests. Bond number-controlled mode. Tests were insufficient for determining the effect on barrier stability of the various dimensionless parameters. From McCarthy (1968) [144].	186
Figure 6-39: Results of dynamic stability tests with different barriers. Bond number-controlled mode. The acceleration, g , is parallel to the barrier. From Fester (1973) [67]. A Reynolds number through the hole has been plotted vs. the critical Bond number.	187
Figure 6-40: Results of barrier dynamic stability tests. Weber number-controlled mode. From McCarthy (1968) [144]. The Weber number in abscissae is normalized with an analytical critical Weber number We_c , which is given in Figure 6-41 below.	188
Figure 6-41: Critical Weber number, We_c , as a function of geometry, l/D , and position of the axis of rotation, L/D . These results have been obtained by use of a potential (incompressible, inviscid, irrotational flow) theory with $O_p \rightarrow 1$, although assuming that the barrier induces a capillary pressure difference. From Gluck (1970) [76].	188

CEN/CLC/TR 17603-31-14:2021 (E)

Figure 6-42: Damping performance of selected barriers. From Fester (1973) [67]. The damping categories A to G are associated to the flow patterns resulting after impingement of the liquid with the barrier, from orderly (A) to irregular (G).....	189
Figure 6-43: Compartmented tank device. From Fester, Eberhardt & Tegart (1975) [68]....	190
Figure 6-44: Sustained liquid height in a capillary tube.	190
Figure 6-45: Sustained ethanol height, l , vs. diameter of fiber, d_o . Gravity level $40g_o$. From Enya, Kisaragi, Ochiai, Sasao & Kuriki (1981) [64].....	191
Figure 6-46: Sustained liquid height, l , vs. gravity level, g/g_o . Liquids are: Ammonia (circle), underfilled Ammonia (square), and ethanol (triangle). Matrix is glass wool, $d_o = 10^{-6}$ m. Solid lines have been deduced from Eq. [6-91] with $\theta = 0$ and the quoted values of d . From Enya, Kisaragi, Ochiai, Sasao and Kuriki (1981) [64].....	192
Figure 6-47: Criterion for the onset of nucleation in subcooled boiling. After Collier (1981) [46].....	193
Figure 6-48: Post height, l , required to position a given ullage, U , under reduced gravity. See Clause 6.4.5.2 for explanation of curves $d/R \neq 0$, B and C.....	194
Figure 6-49: Experimental glass tank with a standpipe. From Petrash, Nussle & Otto (1963) [184]. All the dimensions are in mm.	195
Figure 6-50: Minimum ullage centering capability of the standpipe.....	196
Figure 6-51: Liquid acquisition by the standpipe for large ullages. From Petrash, Nussle & Otto (1983) [184].....	196
Figure 6-52: Central post with thin, off axis, posts (fingers). From Tegart et al. (1972) [233].....	197
Figure 6-53: Criteria to deduce vane profile limits. From Tegart et al. (1972) [233].....	198
Figure 6-54: Limiting vane profiles, R_{min}/R and R_{max}/R for $n = 6, 8$ and 12 vanes. R_{min}/R has been calculated for an ullage $U = 0,05$. R_{max}/R is ullage-independent. After Tegart et al. (1972) [233].	199
Figure 6-55: Simplified bubble geometry. The bubble is held by two contiguous vanes and shapes up as if it were held by the "effective" vane. From Tegart et al. (1972) [233].....	200
Figure 6-56: The ideal distorted axisymmetrical bubble.	201
Figure 6-57: Angle θ_a which measures the distortion of the bubble vs. ratio, R_o/R , of inner body radius to tank radius. Calculated by the compiler.	202
Figure 6-58: Typical effective vane profiles, R_o/R , and dimensionless restoring force, $R\Delta K$, vs. displacement angle, θ . The Figure has been replotted by the compiler after a representation in polar coordinates by Tegart et al. (1972) [233].....	203
Figure 6-59: Typical effective vane profiles, R_o/R , and dimensionless restoring force, $R\Delta K$, vs. displacement angle, θ . The vane profiles have been calculated by Eq. [6-99] with the shown values of k and m . Forces have been deduced from Eqs. [6-96] to [6-98].....	204
Figure 6-60: Bond length, L_b , as a function of T , for saturated Argon, Methane, Nitrogen and Oxygen.....	206
Figure 6-61: Bond length, L_b , as a function of T , for saturated Ethane, Carbon Dioxide and Ammonia.	207

CEN/CLC/TR 17603-31-14:2021 (E)

Figure 6-62: Bond length, L_b , as a function of T , for saturated Hydrogen, Helium and Neon.	208
Figure 6-63: Relation between contact angle, θ , and surface tension, σ , for several liquids on the quoted surfaces.	210
Figure 6-64: Sketch of a dual stage solid cooler. From Nast et al. (1976) [161].	218
Figure 6-65: Liquid helium (He^4) coolers. a) Single stage. b) Dual stage. From Sherman (1978) [216].	219
Figure 6-66: Normal attachment of the VCSs to the cooling duct through heat stationis. From Glaser et al. (1967) [75].	219
Figure 6-67: Tangential attachment of the cooling duct to the shields. Sketched by the compiler after Hopkins & Chronic (1973) [94].	220
Figure 6-68: Detector, T_1 , and optics, T_2 , temperature vs. orbital time.	225
Figure 6-69: JPL-Caltech IR detector cooler arrangement.	227
Figure 6-70: Heat Flow diagram of the Ball Brothers Liquid helium Dewar.	232
Figure 7-1: Phase diagram for He^4 (not to scale). From Arp (1970) [10].	234
Figure 7-2: Schematic of the apparatus used by the Leiden group to produce helium flow through capillaries with independent variation of superfluid and normal velocities. a) From Van der Heijden, Van der Boog & Kramers (1974) [247]. b) From De Haas & Van Beelen (1976) [55].	242
Figure 7-3: The superfluid friction, LF_s , vs. relative velocity, v_n-v_s , for various runs with $\rho_s v_s + \rho_n v_n = \text{Const.}$ From van der Heijden, van der Boog & Kramers (1974) [247].	244
Figure 7-4: The mutual friction, LF_{sn} , vs. relative velocity, v_n-v_s , from various constant mass flux runs. From van der Heijden, van der Boog & Kramers (1974) [247].	245
Figure 7-5: Mutual friction to superfluid friction ratio, F_{sn}/F_s , vs. relative velocity, v_n-v_s , from various runs with $v_s \geq 0$ and $v_n \geq 0$. From van der Heijden, van der Boog & Kramers (1974) [247].	245
Figure 7-6: Isothermal and iso chemical-potential flows in the v_n, v_s plane. The shaded region corresponds to subcritical flow ($\Delta\mu=0$). From van der Heijden, van der Boog & Kramers (1974) [247].	246
Figure 7-7: Correlations between the critical superfluid velocity, v_{sc1} , and the tube diameter, D_E . The experimental data have been re-plotted by the compiler after van Alphen et al. (1969) [246]. They correspond to widely different flow conditions. * Clow and Reppy, $T_\lambda - T \approx 50 \times 10^{-3}$ K. \odot Fokkens, film flow. \blacktriangle Pellman, "superfluid wind tunnel". \square Chase, heat conduction $T \rightarrow T_\lambda$; $v_n \rightarrow 0$. \triangle Van Alphen, adiabatic flow rate. \circ Van Alphen, energy dissipation technique. \blacktriangledown Kramers, second sound attenuation in pure superfluid flow. \bullet Van Alphen, critical flow through jeweller's rouge. ∇ Keller and Hammel, isothermal flow. \bullet Data from reviews of Atkins, and Hammel and Keller.	248
Figure 7-8: Schematic of pressure and temperature drop data as a function of heat flux.	249
Figure 7-9: Schematic of $L_v^{1/2} D_E$ vs. $v_s D_E$ under steady-state conditions. From Childers & Tough (1976) [44].	251
Figure 7-10: Critical Reynolds number for counterflow heat exchange, Re_c , as a function of temperature, T . From Arp (1970) [10].	253

CEN/CLC/TR 17603-31-14:2021 (E)

Figure 7-11: Diagrams which relate the thermal gradient, dT/dx , to the heat flux, q , in counterflow heat exchange. $T=1,5$ K to 2 K. Calculated by the compiler after Arp (1970) [10].	254
Figure 7-12: Temperature profile along a channel filled with He II at atmospheric pressure in conterflow heat exchange. From Bon Mardion, Claudet & Seyfert (1979) [26].	256
Figure 7-13: Tube and He II bath arrangement.	258
Figure 7-14: Film and bulk liquid configuration	259
Figure 7-15: Bernoulli thinning. The full line corresponds to Eq. [7-46]. The dotted line is the Kontorovich (1956) [125] solution. Neither solution gives the correct transition of the film interface to the horizontal free surface in the reservoir, because capillary pressure has been neglected. Curves labelled with the values of Bo correspond to Eq. [7-49].	262
Figure 7-16: Cell used to perform reduced-gravity test. The film thickness experiments were performed in the left hand side compartment. From Yang & Mason (1980) [268].	267
Figure 7-17: Kapitza conductance, h_k , of low Debye temperature metals, Mercury, Lead, Gold and Silver in contact with Liquid Helium, vs. temperature, T . See Table 7-2 below.	273
Figure 7-18: Kapitza conductance, h_k , of Copper in contact with various low acoustic impedance materials vs. temperature, T . See Table 7-2 and Table 7-41 below. Theoretical results are also shown in this figure.	274
Figure 7-19: Kapitza conductance, h_k , of Tungsten, Aluminium, Molybdenum and Beryllium, in contact with Liquid Helium, vs. temperature, T . See Table 7-2 below.	275
Figure 7-20: Kapitza conductance, h_k , of Nonmetals in contact with Liquid helium vs. temperature T . See Table 7-32 below.	275
Figure 7-21: The neutral stability curve for Taconis oscillations when $\xi = 1$. $\circ D_E = 2,4 \times 10^{-3}$ m, $T_H = 288$ K; $\bullet D_E = 2,4 \times 10^{-3}$ m, $T_H = 77,3$ K; $\square D_E = 4,4 \times 10^{-3}$ m, $T_H = 288$ K; $\blacksquare D_E = 4,4 \times 10^{-3}$ m, $T_H = 77,3$ K From Yazaki, Tominaga & Narahara (1979) [269].	304
Figure 7-22: Device for preventing Taconis oscillations. All the dimensions are in mm. From Hilal & McIntosh (1976) [88].	305
Figure 7-23: Superfluid plug arrangement. The intake face of the plug is located at $x = 0$.	306
Figure 7-24: Backward pressure, p_2 , as a function of mass flow rate, m , through the plug. Experimental points are from smooth curves by Karr & Urban (1978, 1980) [113] & [114]. The curve shown in the figure and the Reynolds number in the abscissae axis correspond to turbulent flow (neglecting entrance effects, see ECSS-E-HB-31-01 Part 13 clause 7.2.5) in a straight tube of circular cross-section, under the validity of Blasius formula, for the data shown in the insert. Calculated by the compiler.	312
Figure 7-25: Quadrangle of data required in porous plug performance evaluation.	313
Figure 7-26: Mass flow rate, m , vs. pressure drop, p_1-p_2 , for slits of various lengths, t , and two different bath temperatures, T_1 . From Denner et al. (1980) [56].	324
Figure 7-27: Active Phase Separator (APS). From Denner et al. (1982) [57].	325

CEN/CLC/TR 17603-31-14:2021 (E)

Figure 7-28: Three typical positions of the liquid-vapor interface. a) Ideal flow separation. b) Choking. c) Gorter-Mellink flow. From Schotto (1984) [209].	327
Figure 7-29: Temperature distribution within a 4×10^{-2} m thick. Ceramic plug for several pressure differences. $p_2 = 2,55 \times 10^{-3}$ Pa in any case. From Elsner (1973) [63].	329
Figure 7-30: Time constant, b , as a function of heating power, Q , for the plug described by Karr & Urban (1978,1980) [113] & [114] in clause 7.4.2.6. Position of the heaters, H , is also shown in the figure. White circle: upstream heater power-on; blackcircle: upstream heater power-off; white square: heater at the plug exit power-on; black square: heater at the plug exit, power-off. From Karr & Urban (1978,1980) [113] & [114]. There is no consistent difference between power-on and power-off.	329
Figure 7-31: Fraction, f , of liquid mass lost because of pump down vs. final temperature, T_f . Curves labelled REVERSIBLE correspond to Eqs. [7-80] and [7-81] respectively. Experimental results are also shown. From Nicol & Bohm (1960) [168].	339
Figure 7-32: Mass flow rate, m/ρ , required for a refrigerating load of 10^{-2} W as a function of final temperature, T_f , under three different situations. (a) Liquid He ⁴ is continuously supplied at 4,2 K for evaporation. (b) No supply of He ⁴ . (c) Liquid He ³ is continuously supplied at 3,2 K for evaporation. From Nicol & Bohm (1960) [168].	340
Figure 7-33: Superfluid helium filling assembly. Explanation: NV1 to NV4, ruby needle valve; NV5, standard needle valve; V1, remote controlled QSB for flap valve; V2 to V8, standard valves; F1 and F2, external fittings to maintain cleanliness; T1, 120° flexible transfer tube continuous with filling cryostat and having a 4,2 K radiation shield; T2, long flexible transfer tube for filling 4,2 K tank; R1, 4,2 K reservoir and header tank; R2, 1,5 K reservoir. (NV2 is the porous plug seal. NV3 is the gas vent hole seal). From OXFORD INSTRUMENTS (1976) [176].	341
Figure 8-1: Density, ρ , of Saturated Liquid Argon vs. temperature, T . From Johnson (1961) [109].	348
Figure 8-2: Density, ρ , of Saturated Solid Argon vs. temperature, T . From Johnson (1961) [109].	349
Figure 8-3: Density, ρ , of Saturated Liquid Methane vs. temperature, T . From Johnson (1961) [109].	349
Figure 8-4: Density, ρ , of Saturated Solid Methane vs. temperature, T . From Johnson (1961) [109].	350
Figure 8-5: Density, ρ , of Saturated Liquid Ethane vs. temperature, T . From Johnson (1975) [107].	350
Figure 8-6: Density, ρ , of Saturated Liquid Carbon Dioxide vs. temperature, T . From LEFAX [130].	351
Figure 8-7: Density, ρ , of Saturated Solid Carbon Dioxide vs. temperature, T . From LEFAX [130].	351
Figure 8-8: Density, ρ , of Saturated Liquid Hydrogen vs. temperature, T . From Vargaftik (1975) [253].	352
Figure 8-9: Density, ρ , of Saturated Liquid Helium-4 vs. temperature, T . From Johnson (1961) [109].	352

CEN/CLC/TR 17603-31-14:2021 (E)

Figure 8-10: Density, ρ , of Saturated Solid Helium-4 vs. temperature, T . From Johnson (1961) [109].....	353
Figure 8-11: Density, ρ , of Saturated Liquid Helium-3 vs. temperature, T . From Keller (1969) [119].....	353
Figure 8-12: Density, ρ , of Saturated Liquid Helium-3 -along the freezing curve- vs. temperature, T . From Keller (1969) [119].	354
Figure 8-13: Density, ρ , of Saturated Solid Helium-3 vs. temperature, T . From Keller (1969) [119].....	354
Figure 8-14: Density, ρ , of Solid Helium-3 vs. temperature, T . Values of ρ are shown along the melting curve as well as along curves of constant isobaric compressibility. hcp and bcc stand for hexagonal-close-packed and body-centered-cubic phases of Solid Helium-3, respectively. From Straty (1966) [228]. Additional data for a wider temperature range are given in Figure 8-15.....	355
Figure 8-15: Density, ρ , of Solid Helium-3 vs. temperature, T , along the melting-freezing curve. Since Helium-3 samples were contaminated with around 0,2 % of Helium-4, two freezing curves appear. The figure also reveals the existence of another solid phase, cubic-close-packed (ccp), at high pressures. From Sample (1966) [205].	356
Figure 8-16: Density, ρ , of Saturated Liquid Nitrogen vs. temperature, T . From Johnson (1961) [109].....	356
Figure 8-17: Density, ρ , of Saturated Solid Nitrogen vs. temperature, T . From Johnson (1961) [109].....	357
Figure 8-18: Density, ρ , of Saturated Liquid Ammonia vs. temperature, T . From Vargaftik (1975) [253].	357
Figure 8-19: Density, ρ , of Saturated Liquid Neon vs. temperature, T . From Johnson (1961) [109].....	358
Figure 8-20: Density, ρ , of Saturated Solid Neon vs. temperature, T . From Johnson (1961) [109].....	358
Figure 8-21: Density, ρ , of Saturated Liquid Oxygen vs. temperature, T . From Johnson (1961) [109].....	359
Figure 8-22: Specific heat, c_p , of several gases vs. temperature, T . Sources of data, and pressures are: Ar, CO ₂ , H ₂ , N ₂ and O ₂ , from Hilsenrath et al. (1960) [90], 1 atm. CH ₄ and Ne, from Johnson (1961) [109], 1 atm. C ₂ H ₆ from Vargaftik (1975) [253], 105 Pa. He ⁴ from Angus & de Reuck (1977) [6], 10 ⁵ Pa. NH ₃ from Norris et al. (1967) [171], 1 atm. 1 atm = 1,0135x10 ⁵ Pa.	359
Figure 8-23: Specific heat, c_p , of Gaseous Helium-3 vs. the deviation $ T-T_c $ from critical temperature, T_c , along nearly critical isochores. $T < T_c$. ○ Experimental. $c_p = R[2,7-3,7\ln((T_c-T)/T)]$ $T > T_c$. □ Experimental. $c_p = R[0,5-3,7\ln((T-T_c)/T_c)]$ From Keller (1969) [119]. $T_c = 3-324$ K, $R = R/M$ $R = 8,31432$ J.mol ⁻¹ .K ⁻¹ $M = 3,01603 \times 10^{-3}$ kg.mol ⁻¹	360
Figure 8-24: Specific heat, c_p , of Liquid Helium-3, vs. temperature, T , at several pressures. a) is for $p = p_{sat}$, and the shaded zone is enlarged in b). Data in b) are for the following pressures ○ $p = p_{sat}$; $p = p_{sat}$ □ $p = 14,9 \times 10^5$ Pa. $p = 11,7 \times 10^5$ Pa. $\Delta p = 28,3 \times 10^5$ Pa. $p = 27 \times 10^5$ Pa. Data points are from Strongin et al. (1963) [230] and curves from Keller (1969) [119].	361

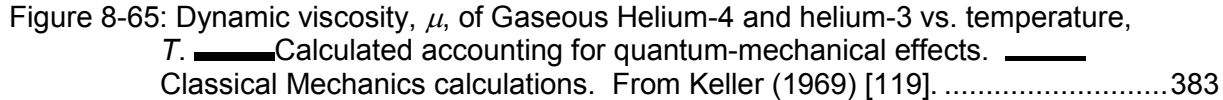
CEN/CLC/TR 17603-31-14:2021 (E)

Figure 8-25: Specific heat, c , of Solid Helium-4 (dashed line) and Solid Helium-3 (full lines), vs. temperature, T . Numbers on the curves are densities in $\text{kg}\cdot\text{m}^{-3}$. From Sample (1966) [205].	362
Figure 8-26: Heat of conversion, h , from Normal to Para Hydrogen vs. temperature, T . From Johnson (1961) [109].	363
Figure 8-27: Heat of vaporization, h_{fg} , of Saturated Liquid Argon vs. temperature, T . From Vargaftik (1975) [253].	363
Figure 8-28: Heat of vaporization, h_{fg} , of Saturated Liquid Methane vs. temperature, T . From Vargaftik (1975) [253].	364
Figure 8-29: Heat of vaporization, h_{fg} , of Saturated Liquid Ethane vs. temperature, T . From Vargaftik (1975) [253].	364
Figure 8-30: Heat of vaporization, h_{fg} , of Saturated Liquid Carbon Dioxide vs. temperature, T . From Angus, Armstrong & de Reuck (1976) [5].	364
Figure 8-31: Heat of vaporization, h_{fg} , of Saturated Liquid Normal Hydrogen vs. temperature, T . From Johnson (1961) [109].	365
Figure 8-32: Heat of vaporization, h_{fg} , of Saturated Liquid Helium-4 vs. temperature, T . From Angus & de Reuck (1977) [6].	365
Figure 8-33: Heat of vaporization, h_{fg} , of Saturated Liquid Helium-3 vs. temperature, T . From Keller (1969)[119].	366
Figure 8-34: Heat of vaporization, h_{fg} , of Saturated Liquid Nitrogen vs. temperature, T . From Johnson (1961) [109].	366
Figure 8-35: Heat of vaporization, h_{fg} , of Saturated Liquid Ammonia vs. temperature, T . From Vargaftik (1975) [253].	366
Figure 8-36: Heat of vaporization, h_{fg} , of Saturated Liquid Neon vs. temperature, T . From Johnson (1961) [109].	367
Figure 8-37: Heat of vaporization, h_{fg} , of Saturated Liquid Oxygen vs. temperature, T . From Johnson (1961) [109].	367
Figure 8-38: Heat of sublimation, h_{fg} , of several solid cryogenics vs. temperature, T . T is bounded from above by the triple point and from below by a vapor pressure of 1,33 Pa. From Nast, Barnes & Wedel (1976) [161].	368
Figure 8-39: Vapor pressure, p_{sat} , of Liquid Argon vs. temperature, T . From Hilsenrath et al. (1960) [90].	369
Figure 8-40: Vapor pressure, p_{sat} , of Solid Argon vs. temperature, T . From Hilsenrath et al. (1960) [90].	369
Figure 8-41: Vapor pressure, p_{sat} , of Liquid Methane vs. temperature, T . From Johnson (1961) [109].	370
Figure 8-42: Vapor pressure, p_{sat} , of Solid Methane vs. temperature, T . From Johnson (1961) [109].	370
Figure 8-43: Vapor pressure, p_{sat} , of Liquid Ethane vs. temperature, T . From Vargaftik (1975) [253].	371
Figure 8-44: Vapor pressure, p_{sat} , of Liquid Carbon Dioxide vs. temperature, T . From Hilsenrath et al. (1960) [90].	371
Figure 8-45: Vapor pressure, p_{sat} , of Solid Carbon Dioxide vs. temperature, T . From Caren & Coston (1968) [36].	372

CEN/CLC/TR 17603-31-14:2021 (E)

Figure 8-46: Vapor pressure, p_{sat} , of Liquid Hydrogen vs. temperature, T . From Vargaftik (1975) [253].	372
Figure 8-47: Vapor pressure, p_{sat} , of Solid Hydrogen vs. temperature, T . From Johnson (1961) [109].	373
Figure 8-48: Vapor pressure, p_{sat} , of Liquid Helium-4 vs. temperature, T . From Angus & de Reuck (1977) [6].	373
Figure 8-49: Vapor pressure, p_{sat} , of Liquid Helium-3 vs. temperature, T . From Mendelssohn (1960) [148].	374
Figure 8-50: Vapor pressure, p_{sat} , of Liquid Nitrogen vs. temperature, T . From Johnson (1961) [109].	374
Figure 8-51: Vapor pressure, p_{sat} , of Solid Nitrogen vs. temperature, T . From Johnson (1961) [109].	375
Figure 8-52: Vapor pressure, p_{sat} , of Liquid Ammonia vs. temperature, T . From Vargaftik (1975) [253].	375
Figure 8-53: Vapor pressure, p_{sat} , of Solid Ammonia vs. temperature, T . From Kutateladze & Borishankii (1966) [127].	376
Figure 8-54: Vapor pressure, p_{sat} , of Liquid Neon vs. temperature, T . From Johnson (1961) [109].	376
Figure 8-55: Vapor pressure, p_{sat} , of Solid Neon vs. temperature, T . From Johnson (1961) [109].	377
Figure 8-56: Vapor pressure, p_{sat} , of Liquid Oxygen vs. temperature, T . From Johnson (1961) [109].	377
Figure 8-57: Thermal conductivity, k , of several gases -at a pressure of 10^5 Pa- vs. temperature, T . From Vargaftik (1975) [253].	378
Figure 8-58: Thermal conductivity, k , of gaseous Carbon Dioxide -at a pressure of 10^5 Pa- vs. temperature, T . From Vargaftik (1975) [253].	378
Figure 8-59: Thermal conductivity, k , of Gaseous Hydrogen and Helium-4 -at a pressure of one atmosphere ($1,013 \times 10^5$ Pa) vs. temperature, T . From Johnson (1961) [109].	379
Figure 8-60: Thermal conductivity, k , of Gaseous Helium-4 and Helium-3 vs. temperature, T . Calculated curves and experimental points are from different sources. From Keller (1969) [119]. The thermal conductivity of Gaseous Helium-4 in a much larger temperature range is given in Figure 8-59.	380
Figure 8-61: Thermal conductivity, k , of Liquid Helium-3 -at several pressures- vs. temperature, T . $\text{---} p = 10^4$ Pa; $\text{—} p = 10^5$ Pa $\text{—} p = 6,7 \times 10^5$ Pa; $\text{—} p = 10^6$ Pa $\text{—} p = 26,9 \times 10^5$ Pa; $\text{—} p = 34,4 \times 10^5$ Pa From Keller (1969) [119].	380
Figure 8-62: Thermal conductivity, k , of gaseous Ammonia -at a pressure of 10^5 Pa- vs. temperature, T . Calculated curves and experimental points are from different sources. From Vargaftik (1975) [253].	381
Figure 8-63: Thermal conductivity, k , of gaseous Neon -at a pressure of one atmosphere ($1,013 \times 10^5$ Pa)- vs. temperature, T . Calculated curves and experimental points are from different sources. From Johnson (1961) [109].	381
Figure 8-64: Dynamic viscosity, μ , of several gases -at a pressure of one atmosphere ($1,013 \times 10^5$ Pa)- vs. temperature, T . All the data are from Johnson (1961)	

CEN/CLC/TR 17603-31-14:2021 (E)

[109] except those corresponding to Argon and Carbon Dioxide which are from Hilsenrath et al. (1960), and those from Ammonia which are from Raznjevic (1970) [190].	382
Figure 8-65: Dynamic viscosity, μ , of Gaseous Helium-4 and helium-3 vs. temperature, T . 	383
Figure 8-66: Dynamic viscosity, μ , of Liquid Helium-3, at several pressures, vs. temperature, T . $\circ p = p_{sat}$, $\square p = 0,23 \times 10^5$ Pa. From Conte (1970) [48] Shaded region enclosed experimental points for $p = p_{sat}$. From Keller (1969) [119]. The line has been calculated from Hone (1962), $p = 0$.	384
Figure 8-67: Prandtl number, $Pr = \mu C_p / k$, of several gases -at a pressure of one atmosphere ($1,0135 \times 10^5$ Pa)- vs. temperature, T . All the data are from Hilsenrath et al. (1960) [90] except those corresponding to Methane, Helium-4, Ammonia and Neon which have been calculated by the compiler.	385
Figure 8-68: Coefficient of linear thermal expansion, β , of Solid Argon vs. temperature, T . From Johnson (1961) [109].	386
Figure 8-69: Coefficient of volumetric thermal expansion (isobaric compressibility), β , of Liquid Nitrogen vs. temperature, T . From Johnson (1961) [109].	386
Figure 8-70: Coefficient of volumetric thermal expansion (isobaric compressibility), β , of Liquid Helium-3 -at pressures near p_{sat} - vs. temperature, T . Curves come from a wide variety of sources, see Keller (1969) [119]. Notice that β is negative in the pressure and temperature ranges under consideration. See also Figure 8-71 for values of β vs. T at the melting curve.	387
Figure 8-71: Coefficient of volumetric thermal expansion (isobaric compressibility), β , of Liquid Helium-3 -at the melting curve- vs. temperature, T . From Straty (1966) [228].	388
Figure 8-72: Coefficient of volumetric thermal expansion (isobaric compressibility), β , of Solid-Helium-3 vs. temperature, T . Numbers on the curves are densities in $\text{kg} \cdot \text{m}^{-3}$. From Straty (1966) [228]. See also Figure 8-14.	388
Figure 8-73: Surface tension, σ , of Saturated Liquid Argon vs. temperature, T . From Johnson (1961) [109].	389
Figure 8-74: Surface tension, σ , of Saturated Liquid Methane vs. temperature, T . From Johnson (1961) [109].	389
Figure 8-75: Surface tension, σ , of Saturated Liquid Ethane vs. temperature, T . From Vargaftik (1975) [253].	389
Figure 8-76: Surface tension, σ , of Saturated Liquid Carbon Dioxide vs. temperature, T . From Kutateladze et al. (1966) [127].	390
Figure 8-77: Surface tension, σ , of Saturated Liquid Normal Hydrogen vs. temperature, T . From Johnson (1961) [109].	390
Figure 8-78: Surface tension, σ , of Saturated Liquid Helium-4 vs. temperature, T . From Johnson (1961) [109].	390
Figure 8-79: Surface tension, σ , of Saturated Liquid Nitrogen vs. temperature, T . From Johnson (1961) [109].	391
Figure 8-80: Surface tension, σ , of Saturated Liquid Ammonia vs. temperature, T . From Dunn & Reay (1976) [61].	391

CEN/CLC/TR 17603-31-14:2021 (E)

Figure 8-81: Surface tension, σ , of Saturated Liquid Neon vs. temperature, T . From Johnson (1961) [109].	391
Figure 8-82: Temperature-entropy diagrams for normal cryogenes. More details are given in Figure 8-83 to Figure 8-94.	394
Figure 8-83: Temperature, T , entropy, s , diagram for Argon. From Vargaftik (1975) [253]. Tabulated values up to $T = 1300$ K and $p = 10^8$ Pa are given in pp. 543 and ff. of the mentioned source. Saturation curve and typical isobars and isochores are shown in the figure.	395
Figure 8-84: Temperature, T , entropy, s , diagram for Methane. From Vargaftik (1975) [253]. Tabulated values up to $T = 1000$ K and $p = 10^8$ Pa are given in pp. 211 and ff. of the mentioned source. Saturation curve and typical isobars and isochores are shown in the figure.	396
Figure 8-85: Temperature, T , entropy, s , diagram for Ethane. From Vargaftik (1975) [253]. Tabulated values up to $T = 500$ K and $p = 5 \times 10^7$ Pa are given in pp. 225 and ff. of the mentioned source. Saturation curve and typical isobars and isochores are shown in the figure.	397
Figure 8-86: Temperature, T , entropy, s , diagram for Carbon Dioxide. From Angus, Armstrong & de Reuck (1976) [5]. Tabulated values up to $T = 1100$ K and $p = 10^8$ Pa are given in pp. 84 and ff. of the mentioned source. Saturation curve and typical isobars and isochores are shown in the figure.	398
Figure 8-87: Temperature, T , entropy, s , diagram for Normal Hydrogen. From Vargaftik (1975) [253]. Tabulated values up to $T = 500$ K and $p = 10^8$ Pa are given in pp. 8 and ff. of the mentioned source. Saturation curve and typical isobars and isochores are shown in the figure.	399
Figure 8-88: Temperature, T , entropy, s , diagram for Parahydrogen. From Vargaftik (1975) [253]. Tabulated values up to $T = 500$ K and $p = 10^8$ Pa are given in pp. 9, and 16 and ff. of the mentioned source. Saturation curve and typical isobars and isochores are shown in the figure.	400
Figure 8-89: Temperature, T , entropy, s , diagram for Helium-4. From Angus & de Reuck (1977) [253]. Tabulated values up to $T = 1400$ K and $p = 7 \times 10^7$ Pa are given in pp. 64 and ff. of the mentioned source. Saturation curve and typical isobars and isochores are shown in the figure.	401
Figure 8-90: Temperature, T , entropy, s , diagram for Helium-3. From Conte (1970) [48]. Only the saturation curve is shown in this figure.	402
Figure 8-91: Temperature, T , entropy, s , diagram for Nitrogen. From Vargaftik (1975) [253]. Tabulated values up to $T = 1300$ K and $p = 10^8$ Pa are given in pp. 433 and ff. of the mentioned source. Saturation curve and typical isobars and isochores are shown in the figure.	403
Figure 8-92: Temperature, T , entropy, s , diagram for Ammonia. From Vargaftik (1975) [253]. Tabulated values up to $T = 560$ K and $p = 1,1 \times 10^8$ Pa are given in pp. 464 and ff. of the mentioned source. Saturation curve and typical isobars and isochores are shown in the figure.	404
Figure 8-93: Temperature, T , entropy, s , diagram for Neon. From Vargaftik (1975) [253]. Tabulated values up to $T = 300$ K and $p = 2 \times 10^7$ Pa are given in pp. 536 and ff. of the mentioned source. Saturation curve and typical isobars and isochores are shown in the figure.	405
Figure 8-94: Temperature, T , entropy, s , diagram for Oxygen. From Vargaftik (1975) [253]. Tabulated values up to $T = 1300$ K and $p = 10^8$ Pa are given in pp.	

CEN/CLC/TR 17603-31-14:2021 (E)

477 and ff. of the mentioned source. Saturation curve and typical isobars and isochores are shown in the figure.	406
Figure 8-95: p - v diagram of a single-component system, illustrating the Maxwell equal area rule.	410
Figure 8-96: The five regions I to V. a) in p, T coordinated, b) in ρ, T coordinates.	428
Figure 8-97: Concentration of normal fluid, ρ_n/ρ , as a function of temperature, T , for bulk He II. ● From Andronikashvili (Mendelssohn (1960) [148]). ○ From values of ρ_s/ρ calculated under the assumption the superfluid critical velocity is temperature independent (van Alphen et al. (1969) [246]).	447
Figure 8-98: Entropy per unit mass, s , of liquid Helium II as a function of temperature, T . — From Dimotakis & Broadwell (1973) [58]. ○ From Broz & Khorana (1976) [31]. From fountain-effect measurements through 5×10^{-7} m pore-size filters.	448
Figure 8-99: Dynamic viscosity, μ_n , of the normal fluid as a function of temperature, T . ○ From Heikkila & Hollis Hallet (1955) [84]. □ From Staas, Taconis & van Alphen (1961) [227]. △ From Woods & Hollis Hallet (1963) [267].	449
Figure 8-100: He ³ to He ⁴ vapor pressure ratio, $p_{\text{satHe3}}/p_{\text{satHe4}}$, vs. temperature, T . Calculated by the compiler after data tabulated in Mendelssohn (1960)	451
Figure 8-101: Specific heat, c , of Silver, Beryllium, Nickel, Stainless Steel and Titanium vs. temperature, T . Details concerning these materials are given below.	453
Figure 8-102: Specific heat, c , of Aluminium and Copper vs. temperature, T . Details concerning these materials are given below.	454
Figure 8-103: Thermal conductivity, k , of Silver, Beryllium, Nickel, Stainless Steel and Titanium vs. temperature, T . Details concerning these materials are given below.	455
Figure 8-104: Thermal conductivity, k , of Aluminium and Copper vs. temperature, T . Details concerning these materials are given below.	456
Figure 8-105: Thermal conductivity, k , of Aluminium alloys vs. temperature, T . Details concerning these materials are given below.	458
Figure 8-106: Thermal conductivity, k , of several Copper alloys vs. temperature, T . Details concerning these materials are given below.	459
Figure 8-107: Total fractional expansion, $\Delta L/L_{293} = (L_{293} - L)/L_{293}$, and coefficient of expansion, $(1/L)(dL/dT)$, of several metallic materials vs. temperature, T . Details concerning these materials are given below.	460
Figure 8-108: Ultimate tensile strength, σ_{ult} , of Aluminium and Copper vs. temperature, T . Details concerning these materials are given below.	462
Figure 8-109: Ultimate tensile strength, σ_{ult} , of Aluminium alloys vs. temperature, T . Details concerning these materials are given below.	463
Figure 8-110: Ultimate tensile strength, σ_{ult} , of a representative copper alloy vs. temperature, T . Details concerning these materials are given below.	464
Figure 8-111: Ultimate tensile strength, σ_{ult} , of Titanium, Titanium alloys and Stainless Steel vs. temperature, T . Details concerning these materials are given below.	465
Figure 8-112: Specific heat, c , vs. temperature, T , of several Glass-Reinforced Composites. From Kasen (1975)a [115].	468

CEN/CLC/TR 17603-31-14:2021 (E)

Figure 8-113: Thermal conductivity, k , vs. temperature, T , of several Glass-Cloth Reinforced Composites. From Kasen (1975)a [115].	469
Figure 8-114: Thermal conductivity, k , in the plane vs. temperature, T , of several Glass-Fiber Reinforced Composites. From Kasen (1975)a [115].	470
Figure 8-115: Thermal expansion, $\Delta L/L$, vs. temperature, T , of several Glass-Fiber Reinforced Composites. From Kasen (1975)a [115].	471
Figure 8-116: Thermal expansion, $\Delta L/L$, normal to the plane, vs. temperature, T , of several Glass-Cloth Reinforced Composites. From Kasen (1975)a [115].	472
Figure 8-117: Thermal expansion, $\Delta L/L$, in the plane, vs. temperature, T , of several Glass-Cloth Reinforced Composites. From Kasen (1975)a [115].	473
Figure 8-118: Ultimate tensile strength, σ_{ult} , vs. temperature, T , of several Glass-Reinforced Composites. From Kasen (1975)a [115].	474
Figure 8-119: Ultimate compressive strength, σ_{ult} , vs. temperature, T , of several Glass-Reinforced Composites. From Kasen (1975)a [115].	475
Figure 8-120: Ultimate flexural strength, σ_{ult} , vs. temperature, T , of several Glass-Reinforced Composites. From Kasen (1975)a [115].	476
Figure 8-121: Specific heat, c , vs. temperature, T , of several Advanced Composites. From Kasen (1975)b [116]. Details concerning these composites are given below.	477
Figure 8-122: Thermal conductivity, k , in the plane, vs. temperature, T , of several Uniaxial Advanced Composites. From Kasen (1975)b [116]. Details concerning these composites are given below.	478
Figure 8-123: In plane, longitudinal thermal expansion, $\Delta L/L$, vs. temperature, T , of several Uniaxial Advanced Composites. From Kasen (1975)b [116]. Details concerning these composites are given below.	480
Figure 8-124: In plane, transverse thermal expansion, $\Delta L/L$, vs. temperature, T , of several Uniaxial Advanced Composites. From Kasen (1975)b [116]. Details concerning these composites are given below.	482
Figure 8-125: Ultimate tensile strength, σ_{ult} , in the plane, vs. temperature, T , of several Uniaxial Graphite-Epoxy Composites. From Kasen (1975)b [116]. Details concerning these composites are given below.	484
Figure 8-126: Ultimate tensile strength, σ_{ult} , in the plane, vs. temperature, T , of several Uniaxial Advanced Composites. From Kasen (1975)b [116]. Details concerning these composites are given below.	486
Figure 8-127: Ultimate compressive strength, σ_{ult} , in the plane, vs. temperature, T , of several Uniaxial Advanced Composites. From Kasen (1975)b [116]. Details concerning these composites are given below.	488
Figure 8-128: Ultimate flexural strength, σ_{ult} , in the plane, vs. temperature, T , of several Uniaxial Graphite-Epoxy Composites. From Kasen (1975)b [116]. Details concerning these composites are given below.	489
Figure 8-129: Ultimate flexural strength, σ_{ult} , in the plane, vs. temperature, T , of several Uniaxial Advanced Composites. From Kasen (1975)b [116]. Details concerning these composites are given below.	491
Figure 8-130: Cost of several fibers (for orders above 50 kg). From Greszczuk et al (1975) [78].	492

CEN/CLC/TR 17603-31-14:2021 (E)

Figure 8-131: Thermal conductivity, k , vs. temperature, T , of several structural tubes. From Foster, Naes & Barnes (1975) [70]. Details concerning these tubes are given below.	493
Figure 8-132: Mechanical and thermal properties of Bone. From Wipf & Gibney (1975) [266]. a) Ultimate compressive strength, σ_{ult} , vs. temperature, T . \circ Values from Armstrong et al. (1971) [9]. \square Values from Wipf & Gibney (1975) [266]. b) Thermal conductivity, k , vs. temperature, T	495
Figure 9-1: Ignition temperature, T_i , of several metals as a function of Oxygen pressure, p . From Clarck & Hust (1974) [45].	506
Figure 9-2: Flash point temperature, T_f , of several nonmetals as a function of Oxygen pressure, p . Also shown the ignition temperature, T_i , of the same materials at high pressure. From Clarck & Hust (1974) [45].	506
Figure 9-3: Effect of pressure in the limits of flammability of natural gas-air mixtures ignited by means of an induction coil. From Lewis & von Elbe (1961) [132].	509
Figure 9-4: Minimum ignition energy, E , and quenching distance, D , for hydrogen-oxygen-inert gas mixtures at atmospheric pressures. From Lewis & von Elbe (1961) [132].	510
Figure 9-5: Dependence of impact energy, J , on temperature, T , for several materials. From Edeskuty, Reider, Williamson (1971) [62].	512
Figure 9-6: Stress intensity at crack arrest, K_{TH} , for AISI 4340 in Hydrogen at ambient temperature, as a function of Hydrogen pressure. From Chandler & Walter (1975) [41].	527
Figure 9-7: Fracture ductility, measured by the tensile reduction in area at fracture, RA , for several steels, as a function of Hydrogen content, CH_2 . From Johnson & Kumnick (1975) [107].	528

Tables

Table 4-1: NASA Mission Categories Requiring Cryogenic Cooling in Space.	42
Table 4-2: Spacecraft Cryogenic Cooling Techniques.	43
Table 5-1: Development Problem Areas of Brayton Cycle Rotary-Reciprocating Refrigerators.	53
Table 5-2: Development Problem Areas of Brayton and Claude Cycle Refrigerators.	55
Table 5-3: Potential Problem Areas Associated with the Stirling Refrigerators.	65
Table 5-4: Development Problem Areas of Vuillemier Cycle Refrigerators.	68
Table 5-5: Maximum Inversion Temperature and Pressure of Selected Cryogenes.	107
Table 6-1: Benefit Obtained from a VCS System in a Storage Container.	122
Table 6-2: Relaxation of the Restrictions Involved in the Idealized Model.	123
Table 6-3: (Effective) Thermal Conductivity of Several MLIs vs. Temperature.	126
Table 6-4: Corrective Factor, ω_n , Giving the Influence of the Number, n , of Conductive Shields on the Boil-off Rate of Several Cryogenes. ($k = \bar{k}$).	133
Table 6-5: Cooled Shield Temperatures, T_i , and Dimensionless Shield Positions, ξ_i , Which Minimize the Boil-off Rate for Several Cryogenes. ($k = k_i T$).	135

CEN/CLC/TR 17603-31-14:2021 (E)

Table 6-6: Cooled Shield Temperatures, T_i , and Dimensionless Shield Positions, ξ_i , Which Minimize the Boil-off Rate for Several Cryogenes. ($k = k_1 T$)	135
Table 6-7: Cooled Shield Temperatures, T_i , and Dimensionless Shield Positions, ξ_i , Which Minimize the Boil-off Rate for Several Cryogenes. ($k = k_1 T$)	136
Table 6-8: Corrective Factor, ω_{nk} , Giving the Influence of the Number, n , of Conductive Shields on the Boil-off Rate of Several Cryogenes. ($k = k_1 T$).....	138
Table 6-9: Figure of Merit, σ/k , of Several Tensile Support Materials at Cryogenic Temperatures ^a	164
Table 6-10: Main Features of Separating Systems for VCS Dewars.....	177
Table 6-11: Phase Separating Systems	178
Table 6-12: Experimental Conditions for Capillary Barrier Stability Studies (Figure 6-37).	185
Table 6-13: Sources of Data for Calculating Bond Lengths	209
Table 6-14: Compatibility of Materials with Ammonia. Non-metals.....	212
Table 6-15: Characteristics of the Lockheed VCS Dewar	222
Table 6-16: Predicted Heat Loads	225
Table 7-1: Several Attempts to Experimentally Verify the Bernoulli Thinning (BT)	265
Table 7-2: Kapitza Conductance, h_k , of Metals in Contact with Liquid Helium (He II).....	276
Table 7-3: Kapitza Conductance, h_k , of Mercury 72 in Contact with Liquid Helium (He II)...	277
Table 7-4: Sample Description of Mercury 72 in Table 7-3	277
Table 7-5: Kapitza Conductance, h_k , of Lead 105 in Contact with Liquid Helium (He II).....	278
Table 7-6: Sample Description of Lead 105 in Table 7-5	279
Table 7-7: Kapitza Conductance, h_k , of Indium 108 in Contact with Liquid Helium (He II)...	280
Table 7-9: Kapitza Conductance, h_k , of Gold 164 in Contact with Liquid Helium (He II).....	281
Table 7-10: Sample Description of Gold 164 in Table 7-9.....	281
Table 7-11: Kapitza Conductance, h_k , of Tin 199 in Contact with Liquid Helium (He II).....	282
Table 7-12: Sample Description of Tin 199 in Table 7-11	282
Table 7-13: Kapitza Conductance, h_k , of Platinum 240 in Contact with Liquid Helium (He II).....	282
Table 7-14: Sample Description of Platinum 240 in Table 7-13	283
Table 7-15: Kapitza Conductance, h_k , of Silver 225 in Contact with Liquid Helium (He II)...	283
Table 7-16: Sample Description of Silver 225 in Table 7-15	284
Table 7-17: Kapitza Conductance, h_k , of Palladium 274 in Contact with Liquid Helium (He II).....	284
Table 7-18: Kapitza Conductance, h_k , of Niobium 275 in Contact with Liquid Helium (He II).....	285
Table 7-19: Sample Description of Niobium 275 in Table 7-18	285
Table 7-20: Kapitza Conductance, h_k , of Copper 343 in Contact with Liquid Helium (He II).....	286
Table 7-21: Sample Description of Copper 343 in Table 7-20	288

CEN/CLC/TR 17603-31-14:2021 (E)

Table 7-22: Kapitza Conductance, h_k , of Tungsten 400 in Contact with Liquid Helium (He II).....	291
Table 7-23: Sample Description of Tungsten 400 in Table 7-22	292
Table 7-24: Kapitza Conductance, h_k , of Aluminium 428 in Contact with Liquid Helium (He II).....	292
Table 7-25: Sample Description of Aluminium 428 in Table 7-24.....	293
Table 7-26: Kapitza Conductance, h_k , of Nickel 450 in Contact with Liquid Helium (He II).....	294
Table 7-27: Sample Description of Nickel 450 in Table 7-26	295
Table 7-28: Kapitza Conductance, h_k , of Molybdenum 450 in Contact with Liquid Helium (He II).....	295
Table 7-29: Sample Description of Molybdenum 450 in Table 7-28.....	296
Table 7-30: Kapitza Conductance, h_k , of Beryllium 1440 in Contact with Liquid Helium (He II).....	296
Table 7-31: Sample Description of Beryllium 1440 in Table 7-30.....	297
Table 7-32: Kapitza Conductance, h_k , of Nonmetals in Contact with Liquid Helium (He II).....	297
Table 7-33: Kapitza Conductance, h_k , of Graphite 420 in Contact with Liquid Helium (He II).....	297
Table 7-34: Sample Description of Graphite 420 in Table 7-33.....	298
Table 7-35: Kapitza Conductance, h_k , of Quartz (SiO ₂) 470 in Contact with Liquid Helium (He II).....	298
Table 7-36: Sample Description of Quartz (SiO ₂) 470 in Table 7-35	298
Table 7-37: Kapitza Conductance, h_k , of Silicon 636 in Contact with Liquid Helium (He II).....	299
Table 7-38: Sample Description of Silicon 636 in Table 7-37.....	299
Table 7-39: Kapitza Conductance, h_k , of Lithium Fluoride 730 in Contact with Liquid Helium (He II).....	300
Table 7-40: Sample Description of Lithium Fluoride 730 in Table 7-39.....	300
Table 7-41: Kapitza Conductance, h_k , of Metals in Contact with Low Acoustic Impedance Media (LAIM)	300
Table 7-42: Kapitza Conductance, h_k , of Indium 108 in Contact with Low Acoustic Impedance Media (LAIM)	301
Table 7-43: Sample Description of Indium 108 in Table 7-42	301
Table 7-44: Kapitza Conductance, h_k , of Copper 343 in Contact with Low Acoustic Impedance Media (LAIM)	302
Table 7-45: Sample Description of Copper 343 in Table 7-44	302
Table 7-46: Variables Characterizing the Porous Media	331
Table 7-47: Expressions Relating the Permeability, K , to Geometrical Properties of the Porous Medium. All expressions in this Table are from Bear (1972) [19].....	333
Table 7-48: Data on Porous Media	335
Table 8-1: Thermodynamic and Transport Properties of Normal Cryogenes	344

CEN/CLC/TR 17603-31-14:2021 (E)

Table 8-2: Thermodynamic and Transport Properties of Normal Cryogenics	345
Table 8-3: Thermodynamic and Transport Properties of Normal Cryogenics	347
Table 8-4: Entropy Departure of Saturated Liquid and Vapor	407
Table 8-5: Values of the Coefficient a_i for Argon.....	413
Table 8-6: Values of the Coefficients a_i , α_n and β_n for Methane	417
Table 8-7: Values of the Coefficients a_i , α_n and β_n for Ethane.....	421
Table 8-8: Values of the Dimensionless Coefficients n_{ij} , a_n and b_n for Carbon Dioxide.....	424
Table 8-9: Values of the Dimensionless Coefficients n_{ij} and γ for Helium-4.....	428
Table 8-10: Values of the Coefficient a_i for Nitrogen.....	432
Table 8-11: Values of the Coefficient a_i for Neon.....	438
Table 8-12: Values of the Coefficient a_i for Oxygen	442
Table 8-13: Relevant Properties of He II as a Function of Temperature	444
Table 9-1: Relevant properties of Cryogen	499
Table 9-2: Several Useful Definitions.....	501
Table 9-3: Thermal Data of Relevant Materials in an Oxidizing Atmosphere	503
Table 9-4: Ranking of Materials for Oxygen Compatibility	507
Table 9-5: Properties of H ₂ and CH ₄ Related to their Combustion Hazards	508
Table 9-6: Symptoms of O ₂ Deficiency	511
Table 9-7: Sources of Mechanical Properties of Structural Alloys at Cryogenic Temperatures.....	512
Table 9-8: SOURCES OF MECHANICAL PROPERTIES OF STRUCTURAL ALLOYS (ALUMINIUM ALLOYS) AT CRYOGENIC TEMPERATURES	513
Table 9-9: SOURCES OF MECHANICAL PROPERTIES OF STRUCTURAL ALLOYS (IRON BASE ALLOYS) AT CRYOGENIC TEMPERATURES.....	515
Table 9-10: SOURCES OF MECHANICAL PROPERTIES OF STRUCTURAL ALLOYS (NICKEL BASE ALLOYS) AT CRYOGENIC TEMPERATURES.....	516
Table 9-11: SOURCES OF MECHANICAL PROPERTIES OF STRUCTURAL ALLOYS (STAINLESS STEELS, AUSTENITIC) AT CRYOGENIC TEMPERATURES....	517
Table 9-12: SOURCES OF MECHANICAL PROPERTIES OF STRUCTURAL ALLOYS (STAINLESS STEELS, MARTENSITIC) AT CRYOGENIC TEMPERATURES.....	519
Table 9-13: SOURCES OF MECHANICAL PROPERTIES OF STRUCTURAL ALLOYS (STEELS) AT CRYOGENIC TEMPERATURES	519
Table 9-14: SOURCES OF MECHANICAL PROPERTIES OF STRUCTURAL ALLOYS (TITANIUM ALLOYS) AT CRYOGENIC TEMPERATURES	521
Table 9-15: Susceptibility of Metals to Hydrogen Embrittlement as Measured by Tensile Tests ^a	523

European Foreword

This document (CEN/CLC/TR 17603-31-14:2021) has been prepared by Technical Committee CEN/CLC/JTC 5 "Space", the secretariat of which is held by DIN.

It is highlighted that this technical report does not contain any requirement but only collection of data or descriptions and guidelines about how to organize and perform the work in support of EN 16603-31.

This Technical report (TR 17603-31-14:2021) originates from ECSS-E-HB-31-01 Part 14A.

Attention is drawn to the possibility that some of the elements of this document may be the subject of patent rights. CEN [and/or CENELEC] shall not be held responsible for identifying any or all such patent rights.

This document has been prepared under a mandate given to CEN by the European Commission and the European Free Trade Association.

This document has been developed to cover specifically space systems and has therefore precedence over any TR covering the same scope but with a wider domain of applicability (e.g.: aerospace).

1

Scope

In this Part 14 cooling methods below 100 K are described. These low temperature levels are mainly required by space borne electronic systems operating under very low noise conditions. Details on the materials used and safety factors are given.

The Thermal design handbook is published in 16 Parts

TR 17603-31-01	Thermal design handbook – Part 1: View factors
TR 17603-31-02	Thermal design handbook – Part 2: Holes, Grooves and Cavities
TR 17603-31-03	Thermal design handbook – Part 3: Spacecraft Surface Temperature
TR 17603-31-04	Thermal design handbook – Part 4: Conductive Heat Transfer
TR 17603-31-05	Thermal design handbook – Part 5: Structural Materials: Metallic and Composite
TR 17603-31-06	Thermal design handbook – Part 6: Thermal Control Surfaces
TR 17603-31-07	Thermal design handbook – Part 7: Insulations
TR 17603-31-08	Thermal design handbook – Part 8: Heat Pipes
TR 17603-31-09	Thermal design handbook – Part 9: Radiators
TR 17603-31-10	Thermal design handbook – Part 10: Phase – Change Capacitors
TR 17603-31-11	Thermal design handbook – Part 11: Electrical Heating
TR 17603-31-12	Thermal design handbook – Part 12: Louvers
TR 17603-31-13	Thermal design handbook – Part 13: Fluid Loops
TR 17603-31-14	Thermal design handbook – Part 14: Cryogenic Cooling
TR 17603-31-15	Thermal design handbook – Part 15: Existing Satellites
TR 17603-31-16	Thermal design handbook – Part 16: Thermal Protection System

2 References

EN Reference	Reference in text	Title
EN 16601-00-01	ECSS-S-ST-00-01	ECSS System - Glossary of terms
TR 17603-31-05	ECSS-E-HB-31-01 Part 5	Thermal design handbook – Part 5: Structural Materials: Metallic and Composite
TR 17603-31-07	ECSS-E-HB-31-01 Part 7	Thermal design handbook – Part 7: Insulations
TR 17603-31-08	ECSS-E-HB-31-01 Part 8	Thermal design handbook – Part 8: Heat Pipes
TR 17603-31-09	ECSS-E-HB-31-01 Part 9	Thermal design handbook – Part 9: Radiators
TR 17603-31-13	ECSS-E-HB-31-01 Part 13	Thermal design handbook – Part 13: Fluid Loops

All other references made to publications in this Part are listed, alphabetically, in the **Bibliography**.

koniec náhľadu – text ďalej pokračuje v platenej verzii STN